The Astrophysical Journal, 933:45 (9pp), 2022 July 1 https://doi.org/10.3847/1538-4357/ac6f56

Extreme Solar Flare-driven Short-wave Fadeout Observed by SuperDARN ZHO Radar

X. J. Liu[1], Z. W. Wang[1,2], J. Y. Lu[1], J. J. Liu[2], H. Q. Hu[2], J. Liu[3], Z. J. Hu[2], M. Wang[1], and K. Zhao[1]
[1] Institute of Space Weather, College of Math and Statistics, Nanjing University of Information Science and Technology, Nanjing, People's Republic of China jylu@nuist.edu.cn
[2] MNR Key Laboratory for Polar Science, Polar Research Institute of China, Shanghai, People's Republic of China; liujianjun@pric.org.cn
[3] Institute of Space Sciences, Shandong University, Weihai, People's Republic of China
Received 2021 December 11; revised 2022 May 9; accepted 2022 May 11; published 2022 July 1

Abstract

Based on the observations from the Super Dual Auroral Radar Network at the Zhongshan Station (−74.9 MLAT, 97.2 MLON) and GOES satellites X-ray sensor, we present the first statistical study of the dayside ionospheric short-wave fadeout (SWF) events on the Southern Hemispheric high latitude from the years 2010–2019 and provide a normal characteristic of SWF with onset of 6 minutes 54 s, blackout of 20 minutes 24 s, and recovery of 39 minutes 36 s, respectively. All the SWF events in this work are selected to be caused by extreme flares. The statistical analysis shows both short-type and long-type SWF onset phases. Onset/blackout phase duration of long events is highly correlated with flare duration (0.79, 0.60), the SWF is mainly driven by the flare radiation profile, and the soft X-ray flux rise rate is higher for short-onset events than for most long-onset events, which is the main reason for the difference between the two types of events. In addition, the effect of ionospheric sluggishness on long-onset events also needs to be considered. The relationship between each phase's durations of long SWFs and the effective peak X-ray flux is not obvious. However, the correlation between the integrated effective X-ray flux and the onset/blackout phase duration of long events is significant.

Unified Astronomy Thesaurus concepts: Solar x-ray flares (1816); Photoionization (2060); Earth ionosphere (860)

1. Introduction

High-frequency (3–30 MHz) radio electromagnetic waves are strongly affected by the ionospheric absorption when propagating in the ionosphere. As one of the fastest and most severe solar activities, flares are the main cause of ionospheric absorption (Mitra 1974). The radiation from solar flares in X-ray and extreme ultraviolet (EUV) bands can reach the Earth in about 8 minutes. In addition, the X-ray flux and EUV radiation may increase by several orders of magnitude during flare activity. When these radiations penetrate deep into the Earth's ionosphere, they significantly enhance the ionization of neutral components on the dayside (e.g., Rose & Ziaud-din 1962; Tsurutani et al. 2009; Berngardt et al. 2018). In this case, the conductivity of the dayside ionosphere also increases rapidly (e.g., Donnelly 1976; Rees 1989; Tsurutani et al. 2005; Dmitriev & Yeh 2008).

More specifically, the soft X-rays (SXRs; 0.1–0.8 nm) and EUV radiation primarily increase the ionization effect of the E-region, while the hard X-rays (<0.1 nm) have a greater potential to go deep into the ionospheric D-region and to cause an enhancement in the number density of electrons in the D-region (Brasseur & Solomon 2006; Rees 1989; Bothmer et al. 2007). When the extra X-rays produced by the flare erupt penetrate deeply into the ionosphere, the electron density, electron-ion collision frequency, and electron-neutral particle collision frequency are all higher in the above regions than in the rest of the ionosphere. Thus, when the radio waves propagate through these illuminated regions, their signal energy could be absorbed by electrons colliding with other particles (e.g., Benson 1964; Banks 1966; Beharrell & Honary 2008). This sudden decline in signals caused by solar flares is well known as short-wave fadeout (SWF; Hargreaves 1992; Zolesi & Cander 2014). The study of the SWF characteristics and their relationship with solar flares is significant to the modern society of science and technology, as it has a significant impact on people's daily lives, such as radio links, satellite communication systems, and the Global Navigation Satellite System (GNSS), etc. (Liu et al. 1996).

SWF was discovered for the first time in 1935 (Dellinger 1937). The early statistical studies show a one-to-one correlation between SWF and solar flares, with the occurrence of SWF increasing as solar activity increases (DeMastus & Wood 1960; Hendl & Skrivanek 1973). Additionally, SWF generally occurs about 1–3 minutes after the flare erupts due to the ionospheric sluggishness (Appleton 1953; Chakraborty et al. 2021). The statistical study of SWFs at Boulder, Colorado, from 1980–1987 shows that the average duration of SWFs was approximately 23 minutes, with 58.9% of events lasting less than 14 minutes, 21.4% lasting between 15 and 29 minutes, 4.3% lasting between 30 and 44 minutes, and 3% lasting more than 90 minutes (Dieminger et al. 2012), respectively. In a further study, Wan et al. (2002) found that the rate of change in the ionosphere's total electron content (TEC) caused by flares is proportional to the flare radiation flux and inversely proportional to the solar zenith's Chapman function. Using the observation data from the Super Dual Auroral Radar Network (SuperDARN) Hokkaido radar, Watanabe & Nishitani (2013) suggested that the Doppler characteristics of SWF observed on HF radar are highly correlated with the D-region plasma enhancement and presented a dependence of HF Doppler frequency shift on distance and elevation angle. Based on the northern hemispheric SuperDARN observation, the relationship between the characteristics of SWFs and solar flares has been studied by Chakraborty et al. (2018). However, their statistical results

provided that X-ray peak fluxes cannot accurately characterize the duration of SWF. Fiori et al. (2018) found that the use of SuperDARN data in ionospheric absorption studies was critical for HF radio signal detection, and the combination of HF radar and riometer data could also benefit the assessment and understanding of both auroral absorption and polar cap absorption.

Rogov et al. (2015) discussed the absorption effect of X-ray flux on HF radio wave propagation in the Earth's near-polar region using the D-region Absorption Model (D-RAP) and gave a function of radio frequency and geographic location. Using an electron density model, Siskind et al. (2017) calculated HF absorption and demonstrated that the contribution of low latitude to HF absorption is typically different from the contribution of middle to high latitude. Using the NRL ray-tracing tool MoJo (Modernized Jones Code), Zawdie et al. (2017) compared the absorption effects of two ray-tracing dispersion relations, Appleton–Hartree and Sen–Wyller, and discussed the importance of electron collision frequency in calculating ionospheric attenuation.

However, most of the above studies focused on the northern hemisphere's lower and middle latitudes, while the high-latitude Antarctic ionospheric SWFs have not been fully studied. The effect of solar flares with terrestrial radio transmissions and the geomagnetic field could be significantly different between high and low latitudes. The difference in latitudes, ionospheric features, and footprints of magnetic lines may result in various statistical properties of radar echoes during flare time (Mendillo & Evans 1974; Hunsucker & Hargreaves 2007; Liu et al. 2021). To improve the understanding of the Southern Hemispheric ionospheric absorption in the high latitude, we perform statistical research on SWF events using the ionospheric echo data from the SuperDARN radar at Zhongshan Station in Antarctica.

2. Data and Methods

2.1. SuperDARN Radar

SuperDARN is a global HF radar network operating at frequencies between 8 and 20 MHz, distributed at middle and high latitudes as well as polar regions in both hemispheres. Each radar transmits 16–20 beams to observe the line-of-sight (LOS) component of the plasma velocity. Each beam is divided into 75–110 ranging gates, with a resolution of 45 km and detection from as close as 180 km (Greenwald et al. 1995; Chisham et al. 2007; Nishitani et al. 2019). The SuperDARN Zhongshan radar station is located at a high geomagnetic latitude (Lat: −74.9, Lon: 97.2) (Danskin et al. 2002). Figure 1 illustrates the radar's field of view. The radar's complete scan contains 16 beams, each with an angular interval of approximately 3°.24 between adjacent beams. Each beam has a time resolution of 3 s, a full quick scan time of about 1 minute, and a spatial resolution of 45 km with a maximum detection distance of 3555 km for the fast scan mode. The LOS velocities, power, and spectral width for the interval are obtained from the raw data samples using the FITACF2.5 library contained in version 4.4 of the Radar Software Toolkit (SuperDARN Data Analysis Working Group et al. 2020).

Typically, radar backward scattering signals are classified into two types: ground-based and ionospheric-based backward echoes (e.g., Greenwald et al. 1995). Due to only three events being well-observed from the ground echoes, in this study, we focus on the ionospheric echoes observed from the SuperDARN Zhongshan radar. The investigation by Fiori et al. (2018) shows that the SWF phenomena were both observed in SuperDARN ionospheric and ground echoes, with a shorter duration in the ionospheric data than the ground data. Normally, the ground echoes are characterized by narrow spectral widths and slow Doppler speeds, which have been excluded by the following criteria (Baker et al. 1988): (a) narrow spectral widths ($V_{\rm los} < 30$ m s^{-1}), and (b) slow Doppler speeds ($\Delta v < 35$ m s^{-1}).

2.2. Solar Flare

The 1 minute GOES SXR data (0.1–0.8 nm) was obtained from the National Centers for Environmental Information website (http://www.ngdc.noaa.gov/stp/satellite/goes/dataaccess.html). The information of the flares was from the Solarsoft database (https://www.lmsal.com/solarsoft/latest_/events_/archive.html). It is worth mentioning that the time when the X-ray flux drops to half of its peak marks the end of a flare burst in the database. The SWF events caused by multi-flare bursts are significantly longer than the independent flares (Chakraborty et al. 2019). Thus, we only considered the independent flares events in this work.

The GOES X-ray data is measured on the satellite orbits and the solar zenith angle (SZA) could affect the local flare radiation in the ionosphere. According to Wan et al. (2002), the TEC variations can be used to study the evolution of the effective flare radiation, which is calculated by the following functions:

$$\frac{\partial \mathrm{TEC}_f}{\partial t} = \frac{\eta' I_f}{Ch(\chi)}, \tag{1}$$

$$\Delta\ \mathrm{TEC}_f = \int_{t_1}^{t_2} \frac{\eta' I_f}{Ch(\chi)} dt, \tag{2}$$

where $\frac{\partial \mathrm{TEC}_f}{\partial t}$ represents the rate of change in TEC produced by the flare, I_f is the solar flare radiation flux at the height of the ionosphere, η' is a constant determined by the effective of ionospheric ionization, χ is the SZA, and $Ch(\chi)$ is the Chapman function corresponding to the SZA. When the SZA is less than 90°, $Ch(\chi) \approx 1/\cos(\chi)$ is a good approximation (Wan et al. 2002). The effective radiation from the solar flares is positively correlated with X-ray flux (Liu et al. 2006; Mahajan et al. 2010). On the right side of Equation (1), the SZA used in the functions is measured at the center location of the radar coverage during the flare time, and the $\frac{\eta' I_f}{Ch(\chi)}$ represents the effective peak X-ray flux (peak$\phi_0 * \cos(\chi)$) in Figure 4 (top) of Section 3.3 afterward. In Equation (2), $\int_{t_1}^{t_2} \frac{\eta' I_f}{Ch(\chi)} dt$ represents the increment of the theoretical TEC produced during the flare (t_1-t_2) and is expressed in terms of the effective X-ray flux integral (E*cos(χ)) in Figure 4 (bottom) of Section 3.3 afterward.

2.3. SWF Event Selection and Parameter Processing

Eccles et al. (2005) found that the ionospheric absorption during the SWF is inversely proportional to the square of the radar frequency. Hence, to keep the same frequency of the radar waves, we only use the channel A data (nearly constant at 10.4 MHz) of SuperDARN Zhongshan radar data in this work.

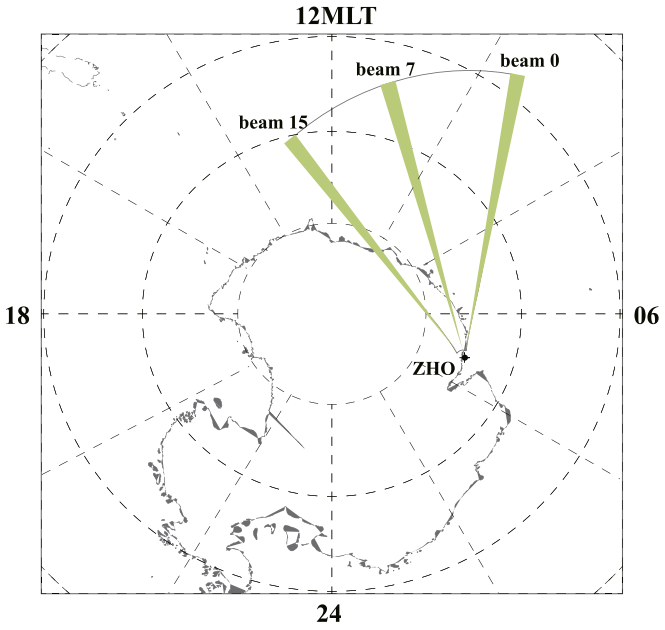

Figure 1. Radar field of view at Zhongshan Station at high latitudes in the Southern Hemisphere.

The full scan (beam 0–15) data is summed as a record so that the radar data has a resolution of 1 minute. For an effective case, the coverage of Zhongshan radar should include exposure to the Sun from the start of the flare to the end of the SWF. The events with $Kp \leqslant 3$ and $AE < 500$ nT were selected to avoid interference from geomagnetic storms and substorm (Chakraborty et al. 2019). Following the above criteria, we statistically analyzed the dayside ionospheric echoes completely attenuated by M- or X-class flares from 2010–2019 during the quiet geomagnetic time.

Normally, the SWF could be divided into three phases: onset, blackout, and recovery. We analyzed ionospheric echoes taking a similar statistical criterion to that of Chakraborty et al. (2018). The 30 minute average of echoes before the onset of the solar flare are used as the background value for each event (e.g., Chakraborty et al. 2018). The onset of SWF is the time when the number of echoes falls to 95% of the background value. The start of the blackout phase is that the number of echoes in this area is less than 15% of the background value. The recovery phase begins with the return of the echo number to 15% of the background value and ends with the return of the echo to the maximum value. Different from Chakraborty et al. (2018), we made minor adjustments during the recovery phase, as the polar ionosphere's complexity made it difficult to restore the radar's ionospheric echoes to their initial level.

Figure 2 is an example of SWF event that meets our criteria. As shown in the three subplots on the top panels of Figure 2, a typical dayside echo absorption event was observed by Zhongshan Station radar on 2012 October 23, during the X1.8 flare. The GOES X-ray is plotted in Figure 2(a). Figure 2(b) shows the ionospheric echoes during the flare. The field-of-view scans of the Doppler velocity in Figures 2 (top left), (top middle), and (top right) were taken 7 minutes apart, with the color label on the left indicating the size and direction of Doppler's line-of-sight speed. The red area represents the plasma moving away from the radar. The blue area is positive values, indicating that the plasma is coming toward the radar. Moreover, the gray area marks ground echoes. The bottom of each subplot is a filled terminator. The yellow region represents the flare's duration as shown in Figure 2(a). It is obvious that the echoes are immediately reduced after the enhancement of the X-ray flux. As shown in Figure 2(b), the number of ionospheric scattering echoes began rapidly declining at 3:15 (UT) and up to the minimum value at 3:17 (UT). This state of echo suppression lasts 4 minutes, resumes at 3:21 (UT), and returns to maximum scattering echoes at 3:36 (UT). Geomagnetic activity levels remain low throughout events, with an average daily *Kp* index of no more than three and a slight change in the *AE* index.

3. Statistical Results

3.1. SWF Statistics List

We counted all 12 SWF events that met the above criteria between 2010 and 2019. Table 1 lists the X-ray flare classes corresponding to the 12 SWF events, including the start time, end time, peak X-ray flux, and SXR rise time received by the GOES satellite. The majority of SWF time occurs between 2013 October and 2014 December, during the peak of the 24th solar cycle. Furthermore, between 2013 October and 2014 December, most of Antarctica experiences polar daylight, smaller SZAs are more conducive to effective X-ray flare ionization of the D- and low E-regions of the dayside ionosphere, which increases the electron density in the photoionization region (Stauning 1996). The durations of the onset, blackout, and recovery phases of the SWF are listed in Columns 4–6 in Table 1.

The short and long duration of the onset are the most noticeable parameters in Table 1. It is certain that there are indeed two SWF events with different durations, which may be influenced by the radiation flux rising rate and ionospheric sluggishness effect. This will be discussed further in Section 4.1. As a result, the outcomes of the two event classifications, onset $\leqslant$120 s (short-onset events, $\leqslant$120 s to express the range of short-onset event durations due to the resolution of 1 minute) and onset $>$120 s (long-onset events), are presented in the following data.

3.2. Relationship between Flare Duration and SWF Duration

Figure 3 shows a scatter plot of the 12 event flare durations in Table 1 versus the onset, blackout, and recovery phases of SWF, and the blue scatter represents short-onset events and the black star-shaped scatter shows long-onset events. The scatter plot in Figure 3(a) depicts the SWF's onset phase and the flare duration. The statistical results show that the onset phase of the long SWF is highly correlated with the flare duration represented by X-rays, with a correlation coefficient of 0.79. Short events do not give any correlation relation because each onset duration is only 2 minutes and the data resolution is 1 minute. The scatter plot of the duration of the blackout phase and the flare for the SWF is shown in Figure 3(b), which demonstrates a high association between the blackout phase and the flare duration (their correlation coefficient is 0.71 for short-onset events and 0.60 for long-onset events). The durations of the SWF recovery phase and the flare are plotted in Figure 3(c), and the correlation coefficient between short-onset events and flare duration is 0.81. The recovery phase duration of the long-onset event has a low correlation with the duration of the flare (0.29). Overall, the duration of each phase of the SWF increases linearly with the flare duration.

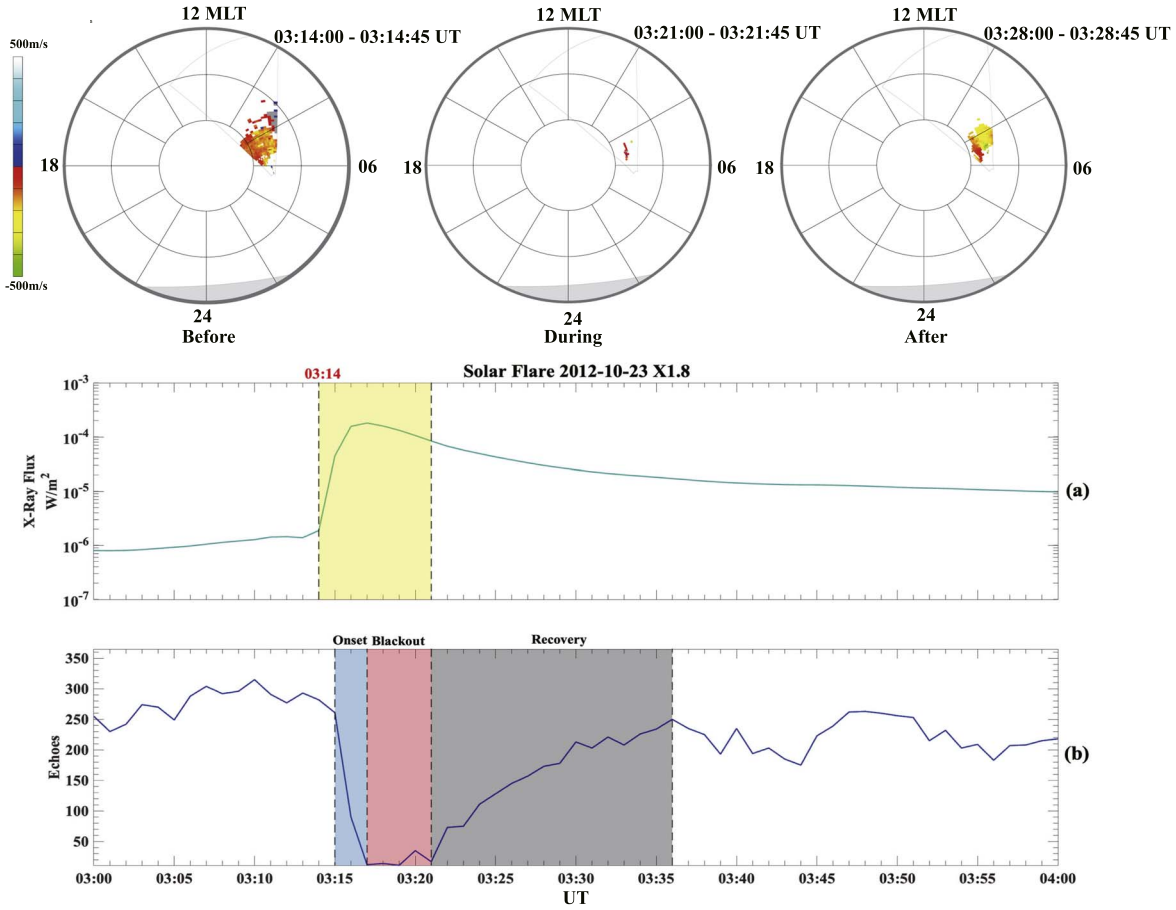

Figure 2. Doppler line-of-sight velocity field-of-view scan as observed by the high-frequency radar at Zhongshan Station (top). Observation data of GOES satellite X-ray sensor and Zhongshan station high-frequency radar during the flare period on 2012 October 23 (bottom). (a) GOES satellite 0.1–0.8 nm wavelength SXRs. (b) The number of ionospheric scattering echoes observed by high-frequency radar at Zhongshan Station. The blue zone is the onset phase, the red zone is the blackout phase, and the black zone is the recovery phase.

Table 1
SWF and Corresponding X-Ray Flares Observed by Radars from 2010–2019

		SXR Flares					SWF		
	Date UT	Flare Class	Start UT	End UT	Flux Peak (10^{-4} W m^{-2})	SXR Rise Time (minutes)	Onset (minutes)	Blackout (minutes)	Recovery (minutes)
Short-onset events	2012 Oct 23	X1.8	0314	0321	1.81	2	2	4	15
	2013 Oct 25	X1.7	0753	0809	1.74	3	2	6	19
	2013 Nov 08	X1.1	0420	0428	1.12	2	2	6	10
	2013 Nov 10	X1.1	0508	0518	1.13	2	2	8	19
	2014 Nov 05	M7.9	0939	0955	0.796	3	2	9	25
Long-onset events	2011 Feb 15	X2.2	0144	0205	2.30	6	6	26	30
	2012 Mar 05	X1.1	0230	0443	1.14	15	15	50	138
	2013 Nov 19	X1.0	1014	1034	1.04	4	7	20	57
	2014 Oct 19	X1.1	0417	0540	1.10	18	14	44	54
	2014 Oct 22	M8.7	0120	0228	0.879	16	13	29	29
	2014 Oct 26	X2.0	1004	1118	2.01	8	7	19	33
	2014 Dec 17	M8.7	0421	0520	0.875	13	11	24	46

3.3. Effect of Effective X-Ray Flux Integration on SWF

The correlation between the SWF's three phase durations and the effective peak X-ray flux for the 12 flare events listed in Table 1 is examined in Figures 4(a)–(c), and the results show that the duration of the three phases of the long-onset event has weak correlation with the effective peak X-ray flux. The duration of the blackout/recovery phase and the effective peak X-ray flux showed a negative correlation for short-onset events. The higher correlation (0.82) for the blackout phase may be a coincidence in that there are too few data points, but the downward trend is the same as the result of the short-onset events of the statistics by Chakraborty et al. (2018). According to Figures 4(d) and (e), the durations of the long event onset and blackout phase have a strong positive correlation with the effective X-ray flux integral, with correlation coefficients of

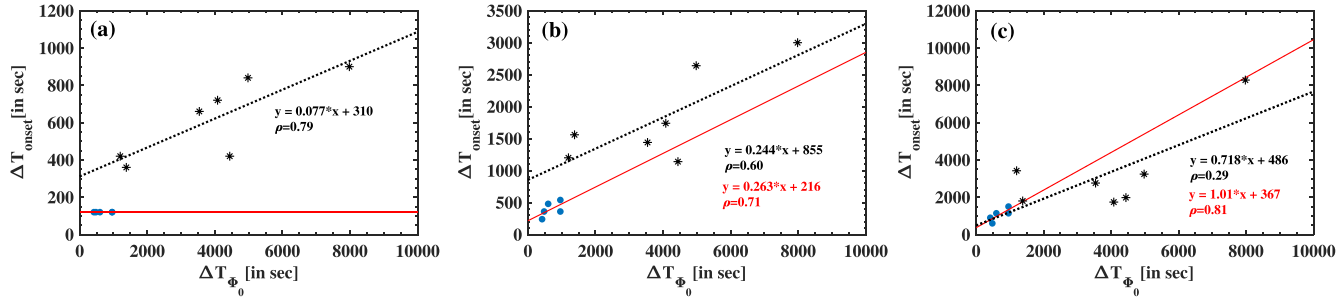

Figure 3. Scatter plot of the three phases' durations in relation to the flare's duration (ΔT_{Φ_0}). Blue scatter points indicate short-onset events, while star-shaped scatter points indicate long-onset events. The long-onset event fitted values are indicated by the black dashed line, the short-onset event fitted values are indicated by the red line, and ρ is the relevant correlation coefficient. (a) Onset phase duration ($\Delta T_{\rm onset}$) and flare duration scatter plot. (b) Blackout phase duration and flare duration scatter plot ($\Delta T_{\rm blackout}$). (c) Recovery phase duration and flare duration scatter plot ($\Delta T_{\rm recovery}$).

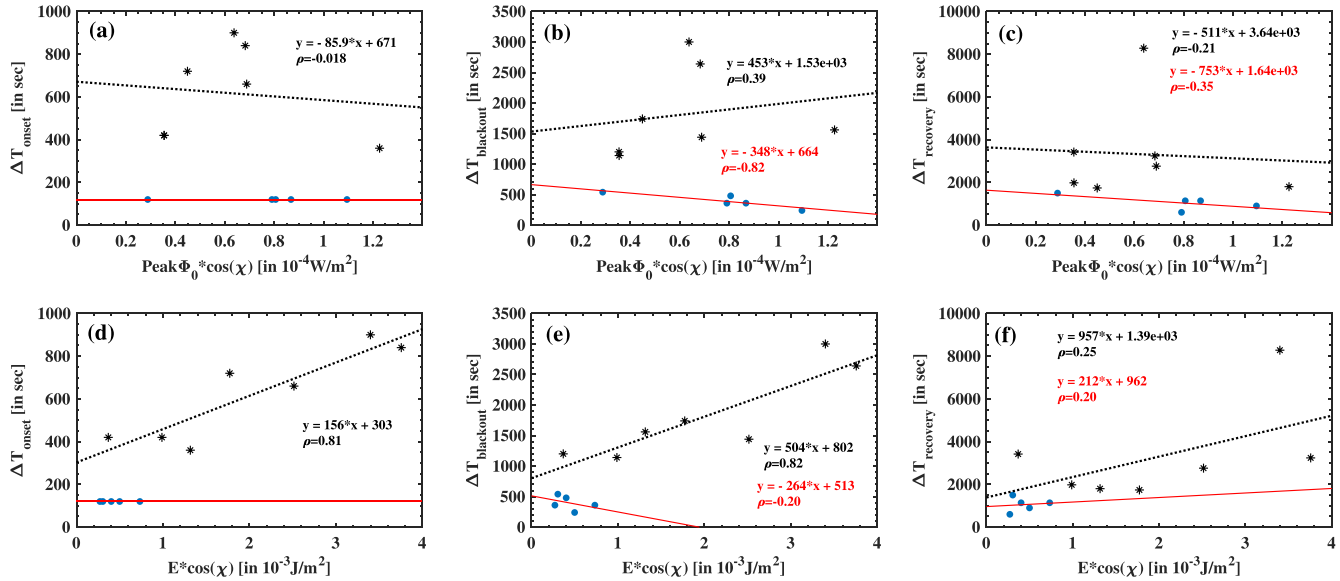

Figure 4. Scatter diagram of effective X-ray peak flux (peakϕ_0*cos(χ)) and the duration of the three phases of SWF ((a)–(c)). Effective X-ray flux integration (E*cos(χ)) and SWF three phases duration scatter plot ((d)–(f)). The blue scatters denote short-onset events, while the black star-shaped scatters indicate long-onset events. The red lines represent the fitted value for short-onset events, while the black dashed lines represent the fitted value for long-onset events.

0.81 and 0.82, respectively; The short-onset event, which blackout phase has a weak correlation with the effective X-ray flux integral, the correlation coefficient is −0.20. As shown in Figure 4(f), the overall recovery phase has a weak correlation with the integral of the effective X-ray flux (correlation coefficient of 0.25 for long-onset events and 0.20 for short-onset events). The recovery phase lasts too long, which may leads to other impact factors of echo recovery duration time except for flares. Although the correlation coefficient for the recovery phase of long-onset events appears low, we think the results of the uptrend are understandable. The longer the flare lasts, the more solar radiation energy will accumulate. This result may imply that the theoretical ionospheric TEC will be larger, which will ultimately increase the duration of the SWF during the blackout (Figures 4(e)) and recovery phases (Figures 4(f)).

3.4. Epoch Analysis of the SWF at Antarctic High-latitude Ionosphere

Figure 5 depicts a superposed epoch analysis of full echo attenuation events listed in Table 1, taking the blackout staring time (blue dashed line) as the key time (0.0 hr). The black line represents the mean value of all the events, and the red standard deviation error bar reflects the fluctuation state. Figures 5(a) and (b) represent the number of ionospheric echoes encoded by flare duration time and effective X-ray flux integration. In Figures 5(a) and (b), the HF absorption features of events below the thick black line (average) are more pronounced, which have darker colors corresponding to longer flare durations and larger effective X-ray integrals. The characteristics of the average duration of SWF at high latitudes in the Antarctic region are depicted in Figure 5(c). The duration of the onset phase is 6 minutes 54 s, the blackout phase lasts 20 minutes 24 s, and the recovery phase lasts 39 minutes 36 s.

4. Discussion

This work focuses on 12 SWF events associated with three M- and nine X-class solar flares detected by the SuperDARN Zhongshan Station HF radar in the absence of geomagnetic interference between 2010 and 2019. As an ionospheric response of the flare, the SWF events mainly occur in the peak duration of solar cycle.

4.1. Possible Explanations for Long- and Short-onset Events

The onset phase is generally within the rising phase of the flare radiation. Naturally, after the ending of the onset phase,

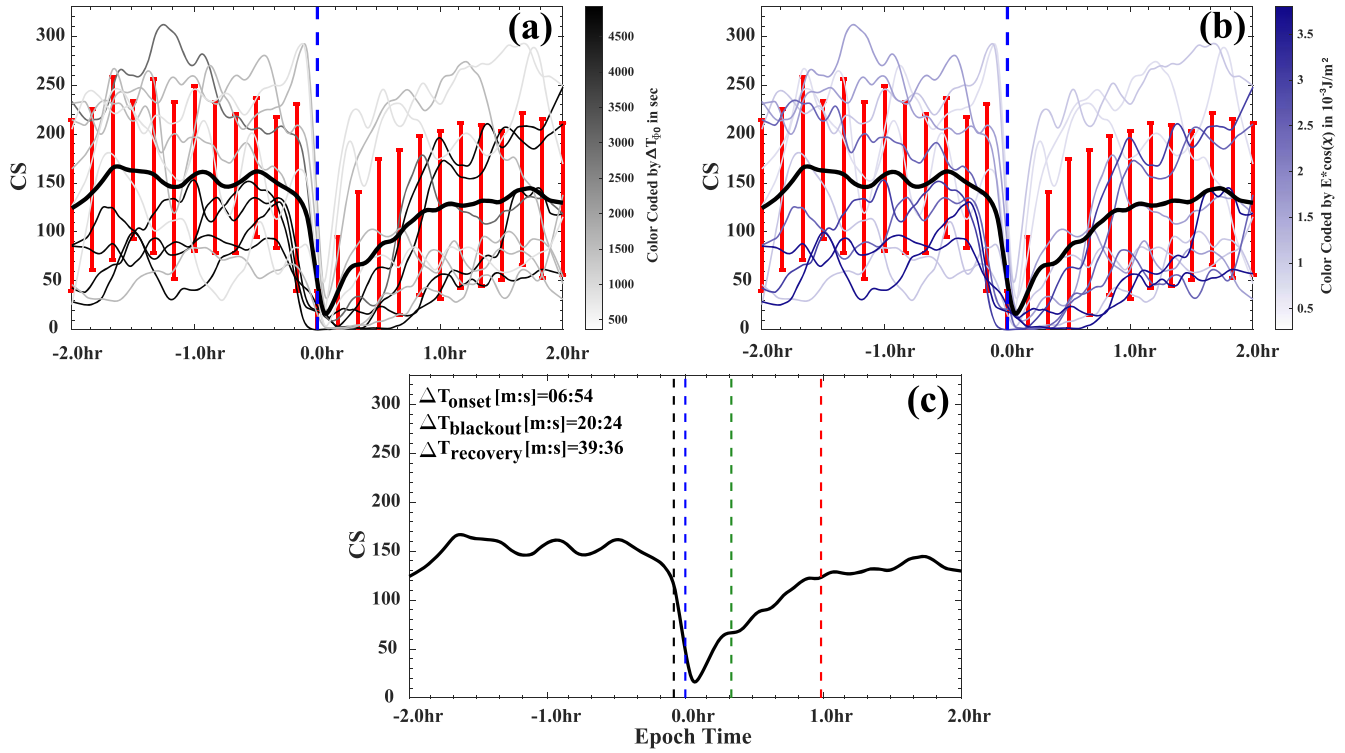

Figure 5. Epoch analysis of the echo signals of the 12 SWF events. (a) Ionospheric scattering echo encoded by the duration of the flare (ΔT_{Φ_0}). (b) Ionospheric scattering echo coded by the effective X-ray flux integral ($E * \cos(\chi)$). (c) The average duration of the three phases of SWF. The black dashed line represents the beginning of echo reduction. The blue dashed line represents the beginning of the blackout, the green dashed line represents the beginning of recovery, and the red dashed line represents the ending of recovery.

the onset phase has no causal relationship with the subsequent effect of the flare. Therefore, the selected effective flare radiation rise time range should be between the beginning of the SXR flux burst (T_{start}) and the end of the onset (T_{end}), which subtracts the estimated ionospheric sluggishness of 1–3 minutes. The association between the average rise rate of SXRs' "K" and onset for all events over this time is compared in Figure 6. It can be found that the K of the short-onset events is larger than most of the long-onset events, which indicates that the rising rate of the flare radiation is an important factor to distinguish the long-/short-onset events. The time variation of the X-ray radiation intensity induces changes in the photo-ionization rate in the D-region (Nina et al. 2018). The quick increase in flare radiation leads to short-onset events that can acquire the required radiant energy absorbed by HF in a short time.

Meanwhile, scatter plots between flare rise time and SWF onset phase for long-onset events are shown in Figures 7(a) and (c) (flare rise time expressed in SXR ($\Delta T_{rs}^{\text{SXR}}$) and EUV ($\Delta T_{rs}^{\text{EUV}}$), respectively). Since higher altitude ionospheric echo data were used, we supplemented EUV data at 26–34 nm (Le et al. 2013). It can be seen a large correlation between the rise time of SXR/EUV and SWF onset time, with correlation coefficients of 0.72 and 0.82. Similarly, from Table 1, one can see the onset time for shorter events is 120 s while the flare rise time is between 2 and 3 minutes. This suggests that X-ray flare temporal dynamics have an impact on the overall shape of SWF observed by HF radars.

In addition, the effect of ionospheric sluggishness on onset needs to be considered. sluggishness should inversely vary with the rate of change of slope of the flux-time profile (Palit et al. 2015). Meanwhile, as shown in Figures 7(b) and (d), Φ_{EUV} and

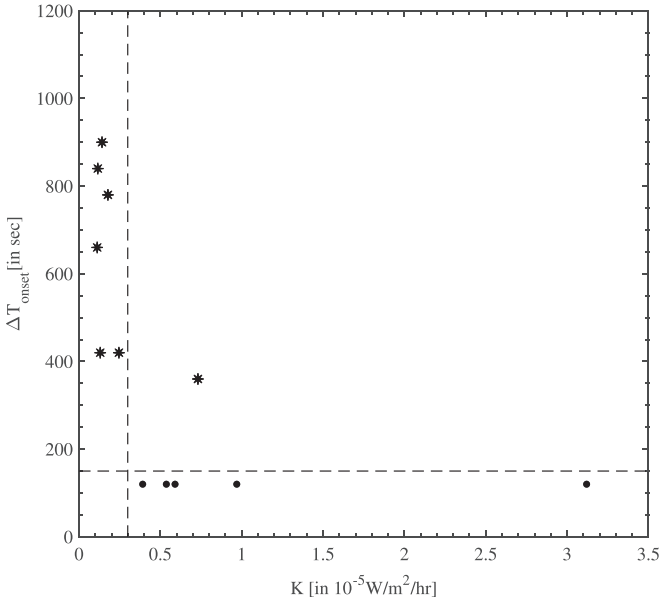

Figure 6. Scatter plots of the ΔT_{onset} vs. K for different SWF events. Star-shaped points are long-onset events, black points are short-onset events. K represents the average rise rate of SXRs.

Φ_{SXR} are the radiant fluxes of EUV/SXR corresponding to all events at time T_{end}, respectively, which is the maximum effective solar irradiance corresponding to the onset phase. Note that in Figure 7(b), an abnormal event marked by a ring is excluded from the fit, which EUV peak solar irradiance even smaller than the initial state of the other events. It can be seen that the long onset and solar irradiance at time T_{end} are

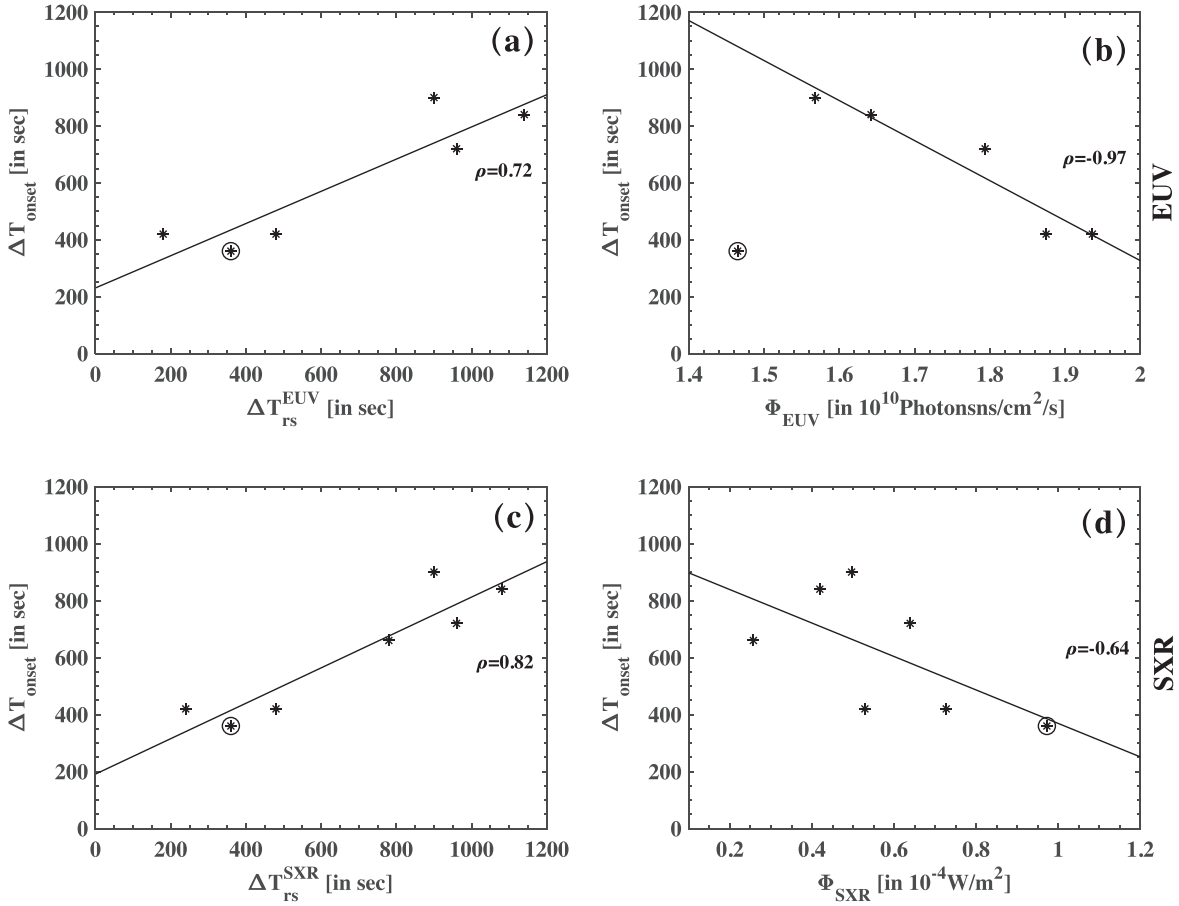

Figure 7. Correlation analysis between the duration of long events ($\Delta T_{\rm onset}$) with (a) EUV rise duration, (b) EUV irradiation at time $T_{\rm end}$, (c) SXR rise duration, and (d) SXR irradiation at time $T_{\rm end}$, respectively. The solid lines represent the linear fitting, the ring is an abnormal event, and ρ is the correlation coefficient.

inversely proportional, with correlation coefficients of (EUV: −0.97, SXR: −0.64), respectively. As discussed by Chakraborty et al. (2021) sluggishness is shown to be anticorrelated with peak solar X-ray flux. Based on reasonable inference, the radiant fluxes and the sluggishness have the same trend at the onset end. This means that for the longer onset event, the sluggishness will make it longer, while the shorter onset received less effect from the sluggishness. The extra time from the sluggishness effect could lead to additional energy injection from the flare. And the radiation curve is rising, even for a short extra time, the additional energy injection at the end of the onset is considerable relative to the previous energy injection. It should be the reason for the high positive correction in Figure 4(d). For the blackout and recovery phases, the extra injection from the sluggishness effect is not obvious relative to their own injection magnitudes.

Thus, the flare-induced SWF phenomena mimics enhanced solar ionization profile. Hence, any delay in ionospheric forcing (long onset, blackout, or recovery) is expected to be primarily driven by the radiation profile. Longer onset time relates to longer flare irradiance rise time, and ionospheric sluggishness is also an essential influence on the onset.

4.2. High-latitude SWF Events in the Southern Hemisphere

The statistical analysis shows that the three phase durations of SWF onset, blackout, and recovery are highly correlated with the duration of flares in high Antarctic latitudes. The results show that the durations of SWF in blackout and recovery phases increase linearly with the enhanced durations of flares.

Among the SWF events estimated by ionospheric echo signals, the average durations of the three phases in the Antarctic region exhibited an onset phase duration of 6 minutes 54 s, a blackout duration of 20 minutes 24 s, and a recovery phase duration of 39 minutes 36 s, respectively. Chakraborty et al. (2018) used ground echoes to count SWFs in the Northern Hemisphere's mid and high latitudes, with the three phases typically lasting 100 s for the onset phase, 10 minutes for the blackout phase, and 42 minutes for the recovery phase. Our duration of the onset phase is longer than that in Chakraborty et al. (2018) and about twice the result of Chakraborty et al. (2018) for the blackout phase. In the recovery phase, the duration of the two results is similar. The difference with the statistical results of Chakraborty et al. (2018) can be explained by the following three points:

1. For all phases, propagation paths are different between ground echoes and ionospheric echoes. For example, a large number of ground echoes were mixed in both the short-onset event (2013 October 25) and the long-onset event (2013 November 19). It is observed that most of the ionospheric echoes disappear after the ground echoes at the onset of these two events but recover before the ground echoes at the recovery phase. This result is consistent with the observations by Fiori et al. (2018) at high latitudes and in the auroral region of the Northern Hemisphere. One of the reasons why ground echoes can

be suppressed more easily than ionospheric echoes may be the times that radar signal passes through the D-region is different. The number of ground echoes passing through the D-region is twice that of the ionospheric echoes passing through the D-region in general, and thus the absorption effect of ground echoes in the ionosphere becomes greater (Watanabe & Nishitani 2013; Chakraborty et al. 2018).
2. For the onset phase, the SXR rise time and ionospheric sluggishness in Section 4.1 may be the main reason for the difference.
3. For the blackout phase, the time is highly positively correlated with the duration of the flare, as illustrated in Figure 3(b). In order to further verify this result, we recalculated the time of the flare events used in Chakraborty et al. (2018) based on the statistical criteria of flare duration described in Section 2.2. The results show that the average duration in Chakraborty et al. (2018) (∼28 minutes) is lower than our average duration (∼43 minutes).

4.3. Advantage of Flare Integration Flux

Combining SZA and X-ray flux is used to correct the absorption effect of the ionosphere. However, the SWF duration exhibits a low response to the effective peak X-ray flux, which is similar to the correlation between the duration of each phase of the SWF and the X-ray flux using ground echo feedback at mid and high latitudes in the Northern Hemisphere (Chakraborty et al. 2018). The reason for this may be that the total ionization effects occurring in the ionosphere cannot be well described only using the peak X-ray flux. Therefore, we make an integral for the X-ray flux during flares. The correlation between the three phases' duration of the long-onset events and the two parameters of the effective X-ray flux integral/effective peak X-ray flux during the flare was compared. It can be seen that the onset/blackout phase duration is highly correlated with the corrected X-ray flux integral, and the performance is significantly better than the effective peak X-ray flux. The duration of both the blackout and recovery phases is proportional to the effective X-ray flux integral. With the increasing of duration of the flare, the effective X-ray flux integral (effective solar radiation) increases, and ultimately the TEC increases due to the photoelectric effect. The increased density of extra electrons may lead to a prolonged blackout and recovery phase. For short-onset events, limited by the duration and number of events, most of the phases show poor correlation with these two parameters.

5. Summary

In this work, we collect the SWF events at high Southern Hemisphere latitudes, and investigate the response of the high Antarctic ionosphere to large solar flare eruptions using ionospheric echoes and flare X-ray fluxes. The results of analysis are as follows:

1. The average duration time of SWF in the Southern Hemisphere are 6 minutes 54 s for the onset, 20 minutes 24 s for the blackout, and 39 minutes 36 s for the recovery.
2. SWF duration is highly correlated to flare duration and increases linearly with increasing flare duration. The integral X-ray flux is a better reflection of SWF duration during the onset and blackout phases than the X-ray peak flux.
3. SWFs were classified as long and short types driven by different flare radiation profiles. In addition, the high inverse correlation between long-onset event duration and peak solar X-ray flux implies that such events may also be influenced by more severe ionospheric sluggishness.

We present the first statistical study of the SWF phenomenon in the Southern Hemisphere high latitude and find that SWF phases are influenced by the rise time of the flare irradiation and ionospheric sluggishness maybe plays a role in this onset phase modulation. In future work, the effect of ionospheric sluggishness on SWF will be examined by analyzing solar irradiance (different bands), latitude, and ionospheric electron density.

The authors acknowledge the use of SuperDARN data (http://vt.superdarn.org). SuperDARN is a collection of radars funded by national scientific funding agencies of Australia, Canada, China, France, Italy, Japan, Norway, South Africa, the United Kingdom, and the United States of America. Zhongshan HF radar as a member of SuperDARN is funded by the Chinese Meridian Project. We thank PRIC (http://www.pric.org.cn) for providing a computing server and SuperDARN data. Raw files can also be accessed via the SuperDARN data mirrors hosted by the British Antarctic Survey (https://www.bas.ac.uk/project/superdarn/#data) and University of Saskatchewan (https://superdarn.ca). We wish to acknowledge the use of the NOAA/GOES X-ray data from (http://www.ngdc.noaa.gov/stp/satellite/goes/dataaccess.html) for flare confirmation and analysis. We are thankful to the SEM/SOHO team for providing the data from the SEM experiment on their website https://dornsifecms.usc.edu/space-sciences-center/download-sem-data/). This work is supported in part by the National Natural Science Foundation of China (grant Nos. 42030203, 41974190, 42074195, and 41974185), the National Key Research and Development Plan of China (2018YFC1407300, 2021YFE0106400), and the Basic Research Institute Stabilization Support Project (A131901W14, A131902W03).

ORCID iDs

X. J. Liu https://orcid.org/0000-0002-7985-3879
Z. W. Wang https://orcid.org/0000-0002-5395-5447
J. Y. Lu https://orcid.org/0000-0001-7042-5395
J. J. Liu https://orcid.org/0000-0003-0465-6210
H. Q. Hu https://orcid.org/0000-0001-8175-5648
J. Liu https://orcid.org/0000-0002-6584-0647
Z. J. Hu https://orcid.org/0000-0003-2448-2094
M. Wang https://orcid.org/0000-0002-3290-8721

References

Appleton, E. V. 1953, JATP, 3, 282
Baker, K. B., Greenwald, R. A., Villian, J. P., & Wing, S. 1988, Interim Rep. Spectral Characteristics of High Frequency (HF) Backscatter for High Latitude Ionospheric Irregularities: Preliminary Analysis of Statistical Properties, Johns Hopkins Univ., Applied Physics Lab
Banks, P. 1966, P&SS, 14, 1085
Beharrell, M., & Honary, F. 2008, JGRA, 113, A05303
Benson, R. F. 1964, RaSc, 68D, 10

Berngardt, O. I., Ruohoniemi, J. M., Nishitani, N., et al. 2018, JASTP, 173, 1
Bothmer, V., Daglis, I. A., & Bogdan, T. J. 2007, PhT, 60, 59
Brasseur, G. P., & Solomon, S. 2006, Aeronomy of the Middle Atmosphere: Chemistry and Physics of the Stratosphere and Mesosphere, Vol. 32 (Berlin: Springer)
Chakraborty, S., Baker, J. B. H., Ruohoniemi, J. M., et al. 2019, SpWea, 17, 1351
Chakraborty, S., Ruohoniemi, J. M., Baker, J. B. H., et al. 2021, JGRA, 126, e28813
Chakraborty, S., Ruohoniemi, J. M., Baker, J. B. H., & Nishitani, N. 2018, RaSc, 53, 472
Chisham, G., Lester, M., Milan, S. E., et al. 2007, SGeo, 28, 33
Danskin, D. W., Koustov, A. V., Ogawa, T., et al. 2002, AnGeo, 20, 1385
Dellinger, J. H. 1937, Proc. IEEE, 25, 1253
DeMastus, H., & Wood, M. 1960, JGR, 65, 609
Dieminger, W., Hartmann, G. K., & Leitinger, R. 2012, The Upper Atmosphere: Data Analysis and Interpretation (Berlin: Springer)
Dmitriev, A. V., & Yeh, H.-C. 2008, JASTP, 70, 1971
Donnelly, R. F. 1976, JGR, 81, 4745
Eccles, J. V., Hunsucker, R. D., Rice, D., & Sojka, J. J. 2005, SpWea, 3, S01002
Fiori, R. A. D., Koustov, A. V., Chakraborty, S., et al. 2018, SpWea, 16, 1348
Greenwald, R. A., Baker, K. B., Dudeney, J. R., et al. 1995, SSRv, 71, 761
Hargreaves, J. K. 1992, The Solar-Terrestrial Environment: An Introduction to Geospace—The Science of The Terrestrial Upper Atmosphere,Ionosphere, and Magnetosphere (Cambridge: Cambridge Univ. Press)
Hendl, R. G., & Skrivanek, R. A. 1973, Environ. Res. Papers, 452, AFCRL-TR–73–0385
Hunsucker, R. D., & Hargreaves, J. K. 2007, The High-latitude Ionosphere and Its Effects on Radio Propagation (Cambridge: Cambridge Univ. Press)
Le, H., Liu, L., Chen, Y., & Wan, W. 2013, JGRA, 118, 576
Liu, J., Wang, W. B., Qian, L. Y., et al. 2021, NatPh, 17, 807
Liu, J. Y., Chiu, C. S., & Lin, C. H. 1996, JGR, 101, 10855
Liu, J. Y., Lin, C. H., Chen, Y. I., et al. 2006, JGRA, 111, A05303
Mahajan, K. K., Lodhi, N. K., & Upadhayaya, A. K. 2010, JGRA, 115, A12330
Mendillo, M., & Evans, J. V. 1974, RaSc, 9, 197
Mitra, A. P. 1974, Ionospheric Effects of Solar Flares, Vol. 46 (Berlin: Springer)
Nina, A., Čadež, V. M., Bajčetić, J., Mitrović, S. T., & Popović, L. Č 2018, SoPh, 293, 64
Nishitani, N., Ruohoniemi, J. M., Lester, M., et al. 2019, PEPS, 6, 27
Palit, S., Basak, T., Pal, S., & Chakrabarti, S. K. 2015, Ap&SS, 356, 19
Rees, M. H. 1989, Physics and Chemistry of the Upper Atmosphere (Cambridge: Cambridge Univ. Press)
Rogov, D. D., Moskaleva, E. V., & Zaalov, N. Y. 2015, AdSpR, 55, 597
Rose, D., & Ziauddin, S. 1962, SSRv, 1, 115
SuperDARN Data Analysis Working Group, Billet, D. D., Bland, E. C., et al. 2020, SuperDARN Radar Software Toolkit (RST) 4.4, Zenodo, doi:10.5281/zenodo.3934368
Siskind, D. E., Zawdie, K. A., Sassi, F., Drob, D., & Friedrich, M. 2017, SpWea, 15, 115
Stauning, P. 1996, JATP, 58, 753
Tsurutani, B. T., Judge, D. L., Guarnieri, F. L., et al. 2005, GeoRL, 32, L03S09
Tsurutani, B. T., Verkhoglyadova, O. P., Mannucci, A. J., et al. 2009, RaSc, 44, RS0A17
Wan, W. X., Yuan, H., Liu, L. B., & Ning, B. Q. 2002, ScChA, 45, 142
Watanabe, D., & Nishitani, N. 2013, Chin. J. Polar Res., 24, 12
Zawdie, K. A., Drob, D. P., Siskind, D. E., & Coker, C. 2017, RaSc, 52, 767
Zolesi, B., & Cander, L. R. 2014, Ionospheric Prediction and Forecasting No. 162-163 (Berlin: Springer)